Static mechanical properties and stress wave attenuation of metaconcrete subjected to impulsive loading

Cheng Xu, Wensu Chen*, Hong Hao*, Thong M. Pham, Kaiming Bi

Centre for Infrastructural Monitoring and Protection,

School of Civil and Mechanical Engineering, Curtin University, Australia

*Corresponding authors: wensu.chen@curtin.edu.au (W. Chen), hong.hao@curtin.edu.au (H. Hao).

Abstract

To mitigate shock wave propagation, a conventional engineered aggregate (EA) consisting of solid core coated with relatively soft material was designed to be tuned at targeted frequencies based on the local resonance mechanism. Previous studies demonstrated that metaconcrete consisting of conventional engineered aggregates (EAs) exhibited favourable attenuation performance of impulsive loading effects on structures. However, it was also found that the existence of the soft coating on conventional EA caused a reduction in the compressive strength of metaconcrete. In this study, a new type of EA by adding a relatively stiff shell outside the soft layer of the conventional EA was developed to overcome the issue of strength reduction whilst keeping its favourable wave attenuation properties. Quasi-static mechanical properties of metaconcrete consisting of conventional and newly developed EAs were examined through standard compression tests. The dynamic responses of the cylindrical metaconcrete specimens subjected to non-destructive and destructive impulsive loadings were also tested to investigate its wave attenuation capacity. The failure processes and the failure modes of metaconcrete made of different types of EAs under destructive tests were compared. It was found that adding a stiffer shell to the conventional EAs can improve the mechanical properties of metaconcrete while still keeping its good performance in mitigating stress wave propagation under both destructive and non-destructive loads.

Keywords: Metaconcrete, Engineered aggregates, Stress wave attenuation, Quasi-static loading, Impulsive loading.

1 Introduction

Concrete structures may experience different types of dynamic loads induced by accidental or natural hazards in their service life, such as earthquakes, wind, accidental explosions and vehicle collisions. Locally resonant metamaterials are the engineered materials designated to manipulate the stress wave propagation, which has excited many researchers' curiosities to apply it for mitigating damage to civil structures [1-5]. In particular, a newly developed concrete-like metamaterial termed as metaconcrete can be used to protect structures from vibration and shock wave loadings due to its favourable wave filtering capacity, which has been intensively investigated in recent years [6-9]. The critical feature associated with metaconcrete is the frequency-dependent attenuation property at the prescribed frequency range induced by the local resonance of engineered aggregate (EA). The conventional EA is made of a solid core coated with a relatively soft layer so that the solid core could oscillate at specific frequencies under dynamic loading. This resonant behaviour triggers the overall system to exhibit negative effective properties (i.e., negative effective mass) interacting with stress waves induced by the dynamic loading. The local oscillation of the solid core could convert the wave energy to its kinetic energy whilst energy imparted by dynamic loads can be absorbed by the embedded resonant aggregates, resulting in the attenuation of stress wave propagation [10-12]. Another feature of metaconcrete is that the tunable frequency range called the "bandgap" can be customized by changing the configuration of resonant aggregates. For instance, Tan et al. [13] numerically investigated the blast wave propagation in the metaconcrete with periodically distributed engineered aggregates coated by different viscoelastic compliant layers for effectively filtering the prescribed frequency range of loading components. In addition, previous experimental studies [14-21] have demonstrated that a metallic core coated with a compliant coating layer could suppress the propagation of waves within the bandgap of metaconcrete. Nevertheless, no experimental study has been conducted yet with respect to the mechanical properties such as the compressive strength of metaconcrete. It is also a lack of experimental verification regarding the effectiveness in mitigating stress wave propagations subjected to destructive impulsive loads. Jin et al. [7] developed high fidelity mesoscale numerical models and performed intensive numerical simulation. The numerical results demonstrated that metaconcrete composed of conventional engineered aggregates (EAs) could reduce the compressive and spalling strengths due to the existence of a soft coating layer. This adverse effect of metaconcrete material may limit its wide applications despite its excellent capability in mitigating wave propagations. No experimental study has been reported in literature yet concerning this issue and a solution to overcome this problem has not yet been developed nor experimentally verified. Therefore, it is deemed necessary to experimentally investigate the mechanical properties of metaconcrete material besides verifying its effectiveness in mitigating stress wave propagations.

To modify the design of conventional engineered aggregates to enhance the strength of metaconcrete and not to lose its wave-filtering capability, engineered aggregates with a relatively stiff layer outside the soft material were developed in this study. Three types of EAs including rubber-coated steel ball (RCSBs), 18 mm rubber-coated steel balls with an additional steel layer (ERCSBs/18) and 15 mm rubber-coated steel balls enclosed in the steel shell (ERCSBs/15) were fabricated, and they were randomly dispersed in cementitious mortar to cast the metaconcrete specimens. Mechanical properties of plain mortar, concrete and metaconcrete with EAs (i.e., RCSBs and ERCSBs) under quasi-static compressive tests and their dynamic responses subjected to impulsive loadings were examined and reported. The influences of adding an enhanced steel layer outside RCSBs on the compressive strength and the wave attenuation performance of metaconcrete were assessed and compared. The frequency spectra obtained from the test data were processed to verify the existence of frequency-dependent wave-filtering capacity. The attenuation mechanism of the metaconcrete with newly proposed ERCSBs was revealed. Furthermore, the effectiveness of metaconcrete in mitigating stress wave propagations induced by destructive impulsive loads with different intensities was investigated. The failure process and failure modes under destructive dynamic loads of metaconcrete specimens of different configurations were compared and discussed.

2 Experiment program

2.1 Specimen preparation

In this study, all specimens can be classified into two groups: mortar-based and concrete-based specimens, the configuration of specimens is schematically illustrated in Fig. 1. S-S1 was made by plain mortar only. S-S2, S-S3 and S-S4 were made of cementitious mortar with 10.6% volume fraction of engineered aggregates (EAs). S-S5 was composed of cementitious mortar and natural aggregates (NAs) of 41.8% in volume. S-S6 and S-S7 consisted of mortar, natural and engineered aggregates. S-S6 contained 31.2% of NAs together with 10.6% of ERCSBs/18. S-S7 included 31.2% of NAs and 10.6% of ERCSBs/15. Namely, the total volume percentage of aggregates (including NAs and EAs) remained 41.8%, while a proportion of natural aggregates (10.6% in total volume) were replaced by respective EAs. To fabricate mortar-based specimens, high strength mortar was utilized as the matrix of metaconcrete. The mortar consisted of Portland cement, fine sand and additives (calcium alumina-sulphate) [22]. The use of high-strength mortar was to provide sufficient strength and avoid potential damage under non-destructive impulsive loadings; hence the enhancement of stress wave attenuation as compared with the plain mortar is mainly due to the local resonance mechanism instead of material damage. The mix ratio of cement/sand/water/additives was 1/2/0.5/0.33. The mix proportions are detailed in Table 1. Natural aggregates with a maximum size of 10 mm and bulk density around 1522 kg/m^3 (in accordance with [23]) were used in the plain concrete mix.

Natural aggregates in combination with engineered aggregates were adopted for concrete-based metaconcrete specimens. When the diameter of a cylindrical specimen is at least three times the maximum size of the natural aggregate, the heterogeneity owing to the existence of aggregates can be neglected in dynamic impact tests [24]. In this study, the diameter of the specimen (i.e., 100 mm) was five times the maximum aggregates size (i.e., 20 mm EAs), therefore the heterogeneity effect under dynamic tests can be neglected.

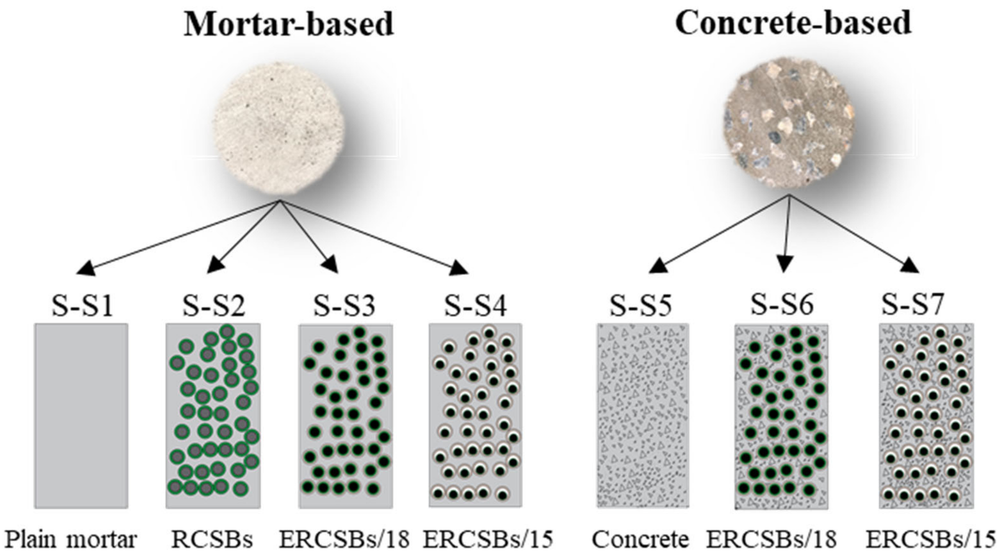

Fig. 1: Specimen classification.

Three types of engineered aggregates (EAs) were utilized to cast metaconcrete specimens including RCSBs (rubber-coated steel balls) and two types of ERCSBs (RCSBs enclosed in a steel shell), i.e., ERCSBs/18 and ERCSBs/15. All EAs were designed to have an identical overall size of 20 mm in diameter. The configuration details of EAs, namely RCSBs and ERCSBs are given in Table 2. Conventional RCSBs were made of steel balls coated with silicone rubber. The dome-shaped rubber coating was prepared by using the moulding technique [20]. The steel ball was then encapsulated by the upper and lower dome-shaped rubber coating, followed by a curing process to form RCSBs. ERCSBs was made by enclosing RCSB with steel shell. Lazar-welding was used to seal steel shell for each ERCSB. Specifically, ERCSBs/18 was made of 18 mm RCSBs with an additional 1 mm-thick steel shell. Besides, inspired by the granular dampers [25-27] and nonlinear spherical pendulum resonator [28], ERCSBs/15 was made by enclosing the RCSB inside a larger steel shell with a gap clearance, i.e., 15 mm diameter RCSB enclosed inside a 20 mm-diameter steel shell. Since the thickness of the steel shell is 1 mm for ERCSBs/15, there is a 3 mm clearance between the steel shell and the RCSB. Under dynamic loading, the RCSB can move inside the steel shell, which also could attract a certain amount of energy induced by the dynamics loading, besides the oscillation of the steel core in conventional EA. Therefore, this type of EA is expected to dissipate the considerable amount of energy via the combination of the motion-caused collisions, sliding and rolling between the inner inclusions and shell walls as well as local vibration of the solid core.

Table 1: Mix proportions.

Type	Water (kg/m^3)	Cement (kg/m^3)	Sand (kg/m^3)	*NA*[b] *(<10mm)* (kg/m^3)	*EA*[c] *(kg/m^3)*	*Additive*[d] (kg/m^3)
Mortar	204	408	816	-	-	136
Plain concrete	204	408	816	863	0	136
Metaconcrete [a]	204	408	816	554	637	136

Note: [a]: concrete-based metaconcrete; [b]: 41.8% volume fraction of natural aggregates (NAs) in plain concrete; [c]: NAs (10.6% in total volume) were replaced by EAs in concrete-based metaconcrete. [d]: Calcium alumina-sulphate was used as the additive.

The metaconcrete specimens were cast in accordance with ASTM C192/C192M-19 [29] using different inclusions such as RCSBs, ERCSBs/18 and ERCSBs/15. Besides, the attenuation mechanism of metaconcrete mainly relied on the local resonance effects of EAs instead of Bragg scattering. Since metaconcrete with randomly distributed EAs tended to be more practical in engineering applications [15], all inclusions (e.g., RCSBs and ERCSBs) were dispersed randomly rather than regular deposition in the cementitious mortar when casting. As listed in Table 3, a total of forty-two cylinders (i.e., six cylinders per configuration) with a height of 200 mm and a diameter of 100 mm were prepared. Plain mortar specimen (S-S1) with

0% EAs was regarded as the reference. In addition, S-S2, S-S3 and S-S4 were fabricated to evaluate the effect of different embedded inclusions on the performance of metaconcrete. Concrete-based specimens (i.e., S-S5 to S-S7) were designed to mix EAs in combination with natural aggregates. Detailed information on the mix proportions, specimens and configuration of EAs is given in Table 2 and Table 3, respectively. A steel rod was used to ram the specimen to minimize the voids during casting. ASTM C192/C192M-19 [29] was followed for the specimen curing.

2.2 Test setup

2.2.1 Quasi-static test

The quasi-static compressive test was conducted by using a MATEST testing machine. The test setup is shown in Fig. 2. For the compressive test, three Ø100 × 200 mm surface-grinded cylinders per configuration were tested with a loading rate of 0.33 MPa/min following the ASTM C39/C39M-21 guide [30] with the equivalent strain rate of 10^{-4} s^{-1}.

Fig. 2: Quasi-static compressive test setup (SG: strain gauge).

Modulus of elasticity and Poisson's ratio were determined based on the guidelines [31]. The longitudinal strain was measured by using the longitudinal strain gauge SG1 attached to the specimen, as shown in Fig. 2. To measure the transverse strain, another strain gauge SG2 with a length of 50 mm was attached perpendicularly to the direction of compression at the middle of the specimen. The reported results are the mean values of three identical specimens. The values of modulus of elasticity and Poisson's ratio can be calculated as follows [31]:

$$E = (S_2 - S_1) / (\varepsilon_2 - 0.000050) \tag{1}$$

where E is chord modulus of elasticity in MPa; S_2 is the stress corresponding to 40% of ultimate load; S_1 is the stress in MPa corresponding to a longitudinal strain ε_1 of 0.000050 and ε_2 is the longitudinal strain produced by stress S_2.

$$\mu = (\varepsilon_{t2} - \varepsilon_{t1}) / (\varepsilon_2 - 0.000050) \tag{2}$$

where μ is Poisson's ratio; ε_{t2} is the transverse strain at mid-height of the specimen produced by stress S_2, and ε_{t1} is the transverse strain at mid-height of the specimen produced by stress S_1.

2.2.2 Dynamic test

In this study, two types of dynamic tests including non-destructive (Fig. 3(a)) and destructive tests (Fig. 3(b)) were carried out. All the dynamic tests were conducted as consistently as possible by using a testing apparatus composed of striker bar, bar I, bar II and bar III with a diameter of 100 mm as well as the buffer system, as shown in Fig. 3. The bars were made of stainless steel with Young's modulus (E_{bar}) of 210 GPa [32]. It is worth noting that the purpose of using this apparatus is not to obtain dynamic material properties, instead, it is to examine the effectiveness in mitigating stress wave propagation of the metaconcrete specimens.

Under the non-destructive test, the impulsive load of the test was generated by manually sliding bar III as a striker to impact bar II, as demonstrated in Fig. 3(a). Two strain gauges (i.e., SG2 and SG3) were attached close to the front and rear surface of the specimen to record the signal, i.e., 30 mm and 170 mm from the incident surface of the specimen, respectively. For the non-destructive test, only the signals of strain gauges attached to the specimen were recorded. The destructive test setup is shown in Fig. 3(b). The striker bar for the destructive test was launched by a pressure vessel to generate intensive dynamic load in order to examine the inelastic response of the specimen. Signal recorded on the bar I was used to determine the input impulsive loads.

A high-speed camera as illustrated in Fig. 3(c) with a frame rate of 12500 frames per second (FPS) was employed to measure the failure process of all specimens under destructive tests. During the destructive tests, rubber pulse shapers with a diameter of 20 mm and thickness of 3 mm were applied to eliminate the high-frequency oscillation as suggested by the previous study [32]. It is worth noting that the specimen was placed between two bars and hanged by two nylon ropes in the actual test setup (Fig. 3(c)). Two nylon ropes were tied near two ends of the specimen. The purpose of using nylon rope was to hold the specimen and align it to the testing apparatus. The specimen using nylon ropes instead of using other supports can minimize unwanted wave dispersion caused by the interaction between the support and stress wave [20].

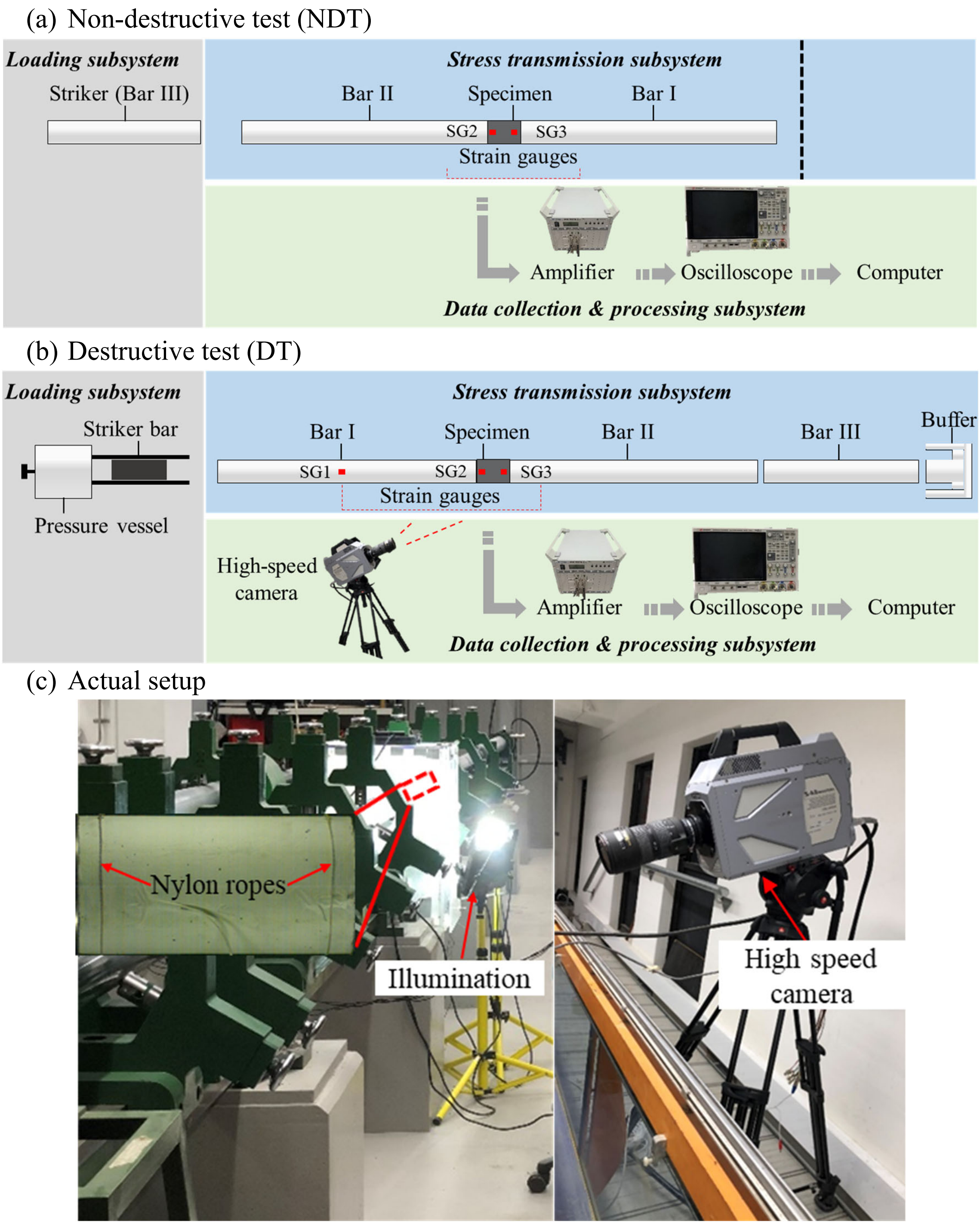

194 Fig. 3: Dynamic test setup.

Table 2: Configuration of engineered aggregates (EAs).

Type	Illustration	Configuration	Dimension	Advantages	Disadvantages
RCSB		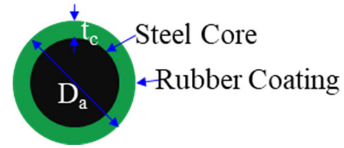	D_a=20 mm t_c=2.3 mm	Local resonance effect	Low stiffness Strength reduction due to the soft coating
ERCSB/18 (no gap)	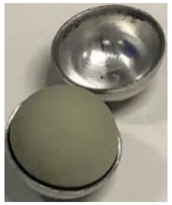	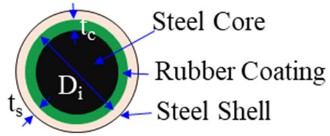	D_a=20 mm D_i=18 mm t_c=1.5 mm t_s=1 mm	Stiffer Local resonance effect	Insufficient bonding due to smooth surface
ERCSB/15 (with a gap)		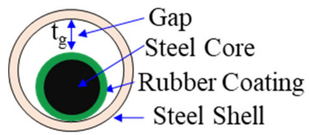	D_a=20 mm D_i=15 mm t_c=1.3 mm t_s=1 mm t_g=3 mm	Stiffer Lighter Local resonance effect Rocking effect	Insufficient bonding due to smooth surface

Note: D_a is the diameter of engineered aggregate; D_i is the diameter of inner inclusion; t_c is the thickness of coating; t_s is the thickness of steel shell; t_g is the gap between RCSB and steel shell.

Table 3: Specimen configurations and test results under non-destructive test (NDT).

Name		Inclusion types	$V_{NA}\%$	$V_{EA}\%$	size (mm)	ρ_{ave} (kg/m^3)	$R_{p\text{-}NDT}$	$R_{s\text{-}NDT}$
S-S1		-	0	-	0	2183.8	-27%	-
S-S2	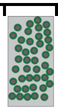	RCSBs	0	10.6%	20	2477.5	79%	396%
S-S3	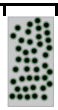	ERCSBs/18	0	10.6%	20	2504.9	86%	422%
S-S4	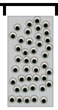	ERCSBs/15	0	10.6%	20	2325.3	62%	332%
S-S5		Natural aggregates (NAs)	41.8%	0	-	2285.7	-0.4%	98%
S-S6	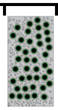	NAs+ ERCSBs/18	31.2%	10.6%	20	2658.9	71%	365%
S-S7	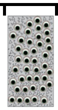	NAs+ ERCSBs/15	31.2%	10.6%	20	2463.9	68%	354%

Note: $V_{NA}\%$ is the volume fraction of natural aggregate; $V_{EA}\%$ is the volume fraction of engineered aggregate; ρ_{ave} is the average density; $R_{p\text{-}NDT}$ is the peak reduction ratio of maximum longitudinal strain; $R_{s\text{-}NDT}$ is the specific reduction ratio of strain with respect to plain mortar (reference). The negative value of the peak reduction ratio means the magnification of amplitude; "-" means reference specimen (S-S1).

3 Results and discussions

3.1 Quasi-static test and results

Fig. 4 shows the failure modes of different specimens under quasi-static compression. Cracks usually initiate at weak locations (e.g., the interface between cement mortar and aggregates, ITZ) and extend into the mortar matrix under quasi-static loading, leading to the brittle failure of the cementitious matrix [33]. Thus, the induced cracks associated with static loading are usually long and have an arbitrary path. The specimen with 0% NAs or EAs (i.e., mortar specimen S-S1) showed a columnar cracking pattern since the specimen was observed to fail into pieces on the external surfaces of the cylinder with brittle collapse, as shown in Fig. 4(a). The failure mode of metaconcrete with 10.6% RCSBs was characterized as a combination of shear and split. Cracks initiating at the top propagated towards the bottom of the specimen and circumferential cracks were bifurcated from a major columnar crack, as highlighted by red circles in Fig. 4(b). Also, there was localized damage around RCSBs as highlighted by the red box in Fig. 4(b) due to the dissimilarity of modulus and deformation between the rubber layer and mortar matrix. Besides, the failure mode of S-S3 was similar to S-S4 with different types of ERCSBs, as shown in Fig. 4(c) and (d). Both S-S3 and S-S4 showed the diagonal shear cracks together with several columnar cracks and failed into more pieces, indicating more severely brittle failure. Meanwhile, columnar vertical cracking through both ends was observed in S-S5 (Fig. 4(e)), and the specimen was broken into pieces. As shown in Fig. 4(f) and (g), the concrete-based metaconcrete specimens (S-S6 and S-S7) had similar failure characteristics as mortar-based metaconcrete specimens. More cracks appeared at the interface between ERCSBs and matrix resulting in localized damages, which might be due to the stress concentration at the interfacial transition zone between ERCSBs and the surrounding matrix.

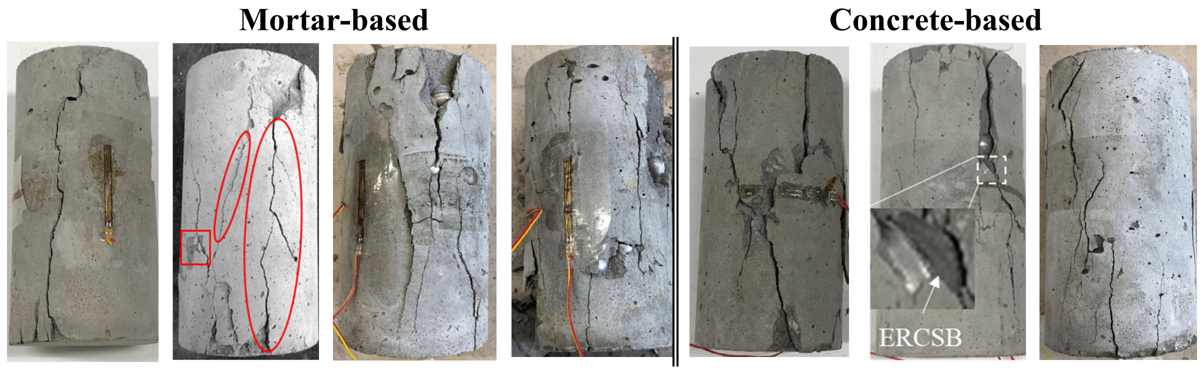

(a) S-S1 (b) S-S2 (c) S-S3 (d) S-S4 (e) S-S5 (f) S-S6 (g) S-S7

Fig. 4: Failure modes of specimens under quasi-static loading.

Fig. 5 shows compressive stress-strain curves for all the specimens under quasi-static tests. All curves show a similar trend and brittle failure after reaching the peak stress. As shown in Fig. 5 (a), the plain mortar S-S1 failed at the average ultimate stress of 67.49 MPa and the average strain at the peak stress was around 0.380%. The plain concrete (S-S5) had an average ultimate strength of 67.92 MPa and the average strain at the peak stress was around 0.352%, as shown in Fig. 5(e). Fig. 5(b), (c), (d), (f) and (g) show the stress-strain curves of metaconcrete specimens. The average strain at the peak stress of metaconcrete S-S2, S-S3, S-S4, S-S6 and S-S7 was about 0.267%, 0.272%, 0.230%, 0.255% and 0.278%, respectively. As observed in Fig. 5, the compressive strength of metaconcrete was considerably improved by using ERCSBs as compared to metaconcrete with RCSBs (S-S2). These results indicated that adding EAs into the concrete mix reduced the concrete strength and deformation ability.

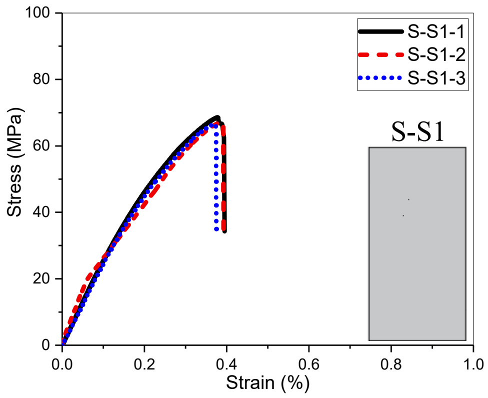

(a) S-S1

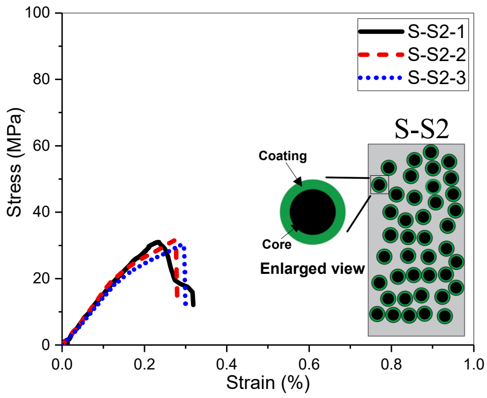

(b) S-S2

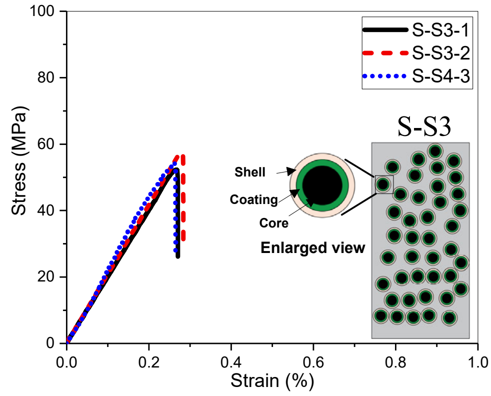

(c) S-S3

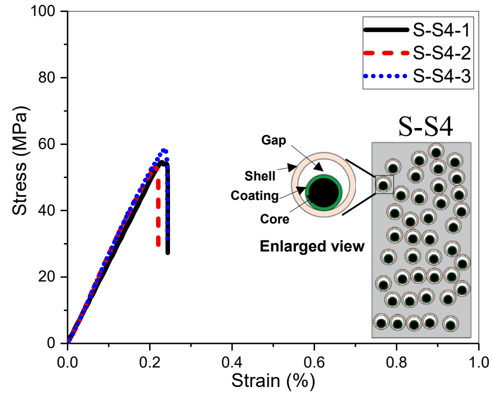

(d) S-S4

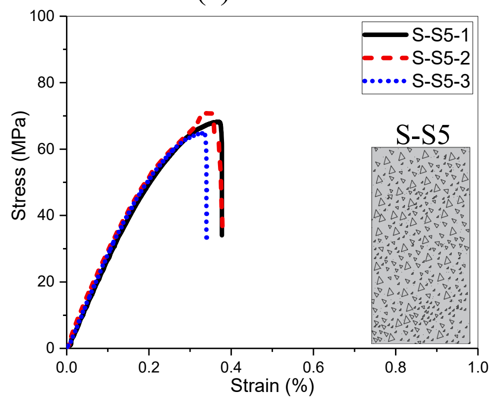

(e) S-S5

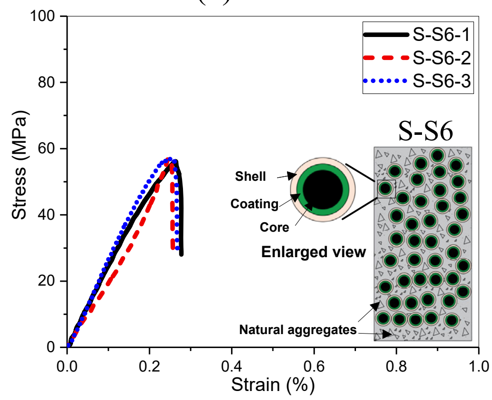

(f) S-S6

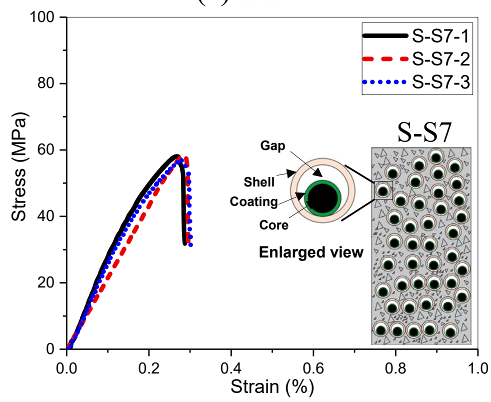

(g) S-S7

Fig. 5: Stress-strain curves of specimens.

The mean compressive strength of mortar and metaconcrete specimens with different aggregate configurations is illustrated in Fig. 6(a). The average compressive strength of S-S1 was 67.49 MPa. However, the compressive strength greatly decreased to 29.98 MPa when adding RCSBs in S-S2. Namely, the reduction in the compressive strength of metaconcrete by adding 10.6% volume percentage of RCSBs was around 55.6% in comparison with S-S1. This result was consistent with that obtained from the detailed numerical modelling [7], i.e., adding RCSBs into the concrete mix could reduce the concrete strength although it local vibrations of the core in RCSBs mitigate stress wave propagation. The reasons for the adverse effect of mixing

RCSBs into the mortar on the compressive strength of metaconcrete were attributed to: a) a soft coating with low stiffness was prone to deform while the surrounding mortar was brittle, causing damage to mortar matrix; b) the mismatch of the elastic modulus and deformation capacity made the surrounding matrix vulnerable to be damaged. As shown, adding a hard steel shell improved the average compressive strength of metaconcrete to 54.97 MPa and 55.57 MPa for S-S3 and S-S4, which increased around 80.3% and 85.4% as compared to S-S2, respectively, but were still lower than the mortar specimen (S-S1). The reason for the compressive strengths of S-S3 and S-S4 being lower than S-S1 was because of the insufficient bonding between the steel shell surface and the surrounding mortar matrix, evidenced by the debonding failure between ERCSBs and mortar matrix shown in Fig. 4. Nevertheless, adding an additional steel shell on the conventional EAs significantly improved the compressive strength of metaconcrete mixed with the conventional EAs. Similar observations can be drawn on the concrete-based specimens, i.e., S5, S6 and S7. The respective average compressive strength was 67.92 MPa, 56.19 MPa, and 56.81 MPa. The strength of metaconcrete with enhanced EAs was still slightly lower than the concrete specimen (S-S5). Therefore, further improvement is deemed necessary to enhance the bonding strength between the EAs and cementitious matrix so that the strength of metaconcrete is not compromised while having the excellent capability of wave propagation mitigation.

The mean modulus of elasticity (E) of the tested specimens is compared in Fig. 6(b) and the average value and standard deviation (SD) are listed in Table 4. The elastic modulus of metaconcrete specimens with conventional EAs was substantially smaller than that of the reference specimen. For instance, the elastic modulus of S-S2 was 15.34 GPa, which was 39.4% lower than that of plain mortar (25.42 GPa). This is again because the soft coating of the conventional EA caused the reduction of the elastic modulus of the metaconcrete. In contrast, the specimens with the enhanced EAs had a comparable or even slightly higher modulus of elasticity than the reference specimen. For instance, by replacing NAs with ERCSBs (i.e., 10.6%

in total volume) in S-S3, S-S4, S-S6 and S-S7, higher modulus of elasticity, i.e., 26.44, 26.59, 26.91 and 26.24 GPa can be obtained, respectively. It is because the steel shell was much stiffer than the surrounding cementitious matrix (i.e., $E_{\mathrm{shell}} >> E_{\mathrm{matrix}}$) and adding a stiff steel shell on the conventional EA overcame the problem of softening the metaconcrete materials. However, the overall modulus of elasticity of metaconcrete with ERCSBs was not changed significantly, implying the elastic modulus was still governed by the mortar matrix.

The mean Poisson's ratio (μ) of the tested specimens is also depicted in Fig. 6(b) and summarized in Table 4. As shown, the mean Poisson's ratio had an opposite variation trend to the modulus of elasticity. All the specimens, except metaconcrete specimens made of conventional EAs, had a similar Poisson's ratio. The Poisson's ratio of the conventional metaconcrete specimen (S-S2) was slightly higher than other specimens. This is because the coating layer outside conventional EAs was made of hyper-elastic material (silicone rubber), which had a higher Poisson's ratio than cementitious mortar.

Table 4 also gives the failure strain (ε_f) and specific fracture energy (G_f) of the specimens. It was found that metaconcrete had lower failure strain and specific fracture energy than plain mortar and concrete in general as metaconcrete had lower deformation capacity and compressive strength due to weak bonding at the EAs-matrix interfaces. Hence, it is essential to enhance the bonding strength between EAs and mortar matrix for improving the performance of metaconcrete. It should be noted that the bonding strength can be improved by using mechanical or chemical treatment such as roughing EAs' surface or adding bonding additives (e.g., epoxy resin) outside the EAs. Alternatively, the steel shell can be replaced by cementitious materials with superior mechanical properties to the surrounding matrix.

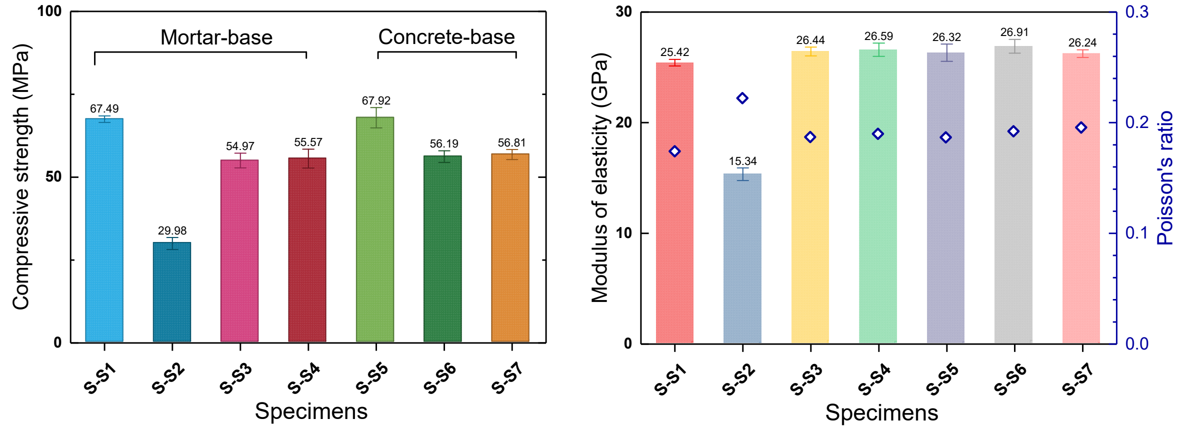

(a) (b)

Fig. 6: Comparisons of (a) Compressive strength; (b) Modulus of elasticity and Poisson's ratio.

Table 4: Mechanical properties of mortar, concrete and metaconcrete specimens.

Specimen No.	f_c^a (MPa)	SD	E^a (GPa)	SD	μ^a	SD	ε_f^a (%)	SD	G_f^a (kJ/m^3)	SD
S-S1	67.49	0.99	25.42	1.01	0.173	0.004	0.380	0.0067	131.02	6.00
S-S2	29.98	1.81	15.34	1.91	0.222	0.003	0.267	0.0241	45.91	1.96
S-S3	54.97	2.22	26.44	1.33	0.187	0.007	0.272	0.0081	81.70	4.36
S-S4	55.57	2.83	26.59	2.00	0.190	0.009	0.230	0.0073	77.50	5.50
S-S5	67.92	3.06	26.32	2.61	0.186	0.005	0.352	0.0142	135.78	9.92
S-S6	56.19	1.78	26.91	2.07	0.192	0.005	0.255	0.0069	82.57	9.40
S-S7	56.81	1.52	26.24	1.17	0.195	0.006	0.278	0.0062	90.01	13.55

Note: ^{a} is 28-days mean value; f_c is compressive strength; E is the modulus of elasticity; μ is Poisson's ratio; ε_f is failure strain; G_f is specific fracture energy, i.e., the enclosed area under the stress-strain curve, in kJ/m^3; SD is standard derivation.

3.2 Dynamic test results and discussion

To quantify the effectiveness of wave propagation mitigation of specimens, three groups of performance metrics were considered in this study. The definition of each performance metric is specified as follows.

(i) $R_{p\text{-}NDT}$ or $R_{p\text{-}DT}$ is defined as the peak reduction ratio of maximum longitudinal strain given by Eq. (3), corresponding to the non-destructive (NDT) or destructive (DT) test. Specifically, it is used to quantify the effectiveness in mitigating stress wave propagation by calculating the ratio of peak strain at the front and rear end of the specimen (i.e., SG2 and SG3), as shown in Fig. 3(a) and (b).

$$R_{p-NDT} \; or \; R_{p-DT} = \left(1 - \frac{\varepsilon_3|_{peak}}{\varepsilon_2|_{peak}}\right) \times 100\% \qquad (1)$$

(ii) $R_{s\text{-}NDT}$ or $R_{s\text{-}DT}$, the specific reduction ratio of strain at SG3 with respect to the reference (S-S1), is computed by Eq. (4).

$$R_{s-NDT}\ or\ R_{s-DT} = (1 - \frac{\varepsilon_{2_{S-Si}}\big|_{peak} / \varepsilon_{3_{S-Si}}\big|_{peak}}{\varepsilon_{2_{S-S1}}\big|_{peak} / \varepsilon_{3_{S-S1}}\big|_{peak}}) \times 100\% \quad where\ i = 1, 2 \cdots 7 \tag{2}$$

(iii) Transmission ratio (TR) is defined as the ratio of output (SG3) to input (SG2) amplitudes in the frequency domain within the specimen by using Eq. (5), which has been used in the previous studies [20, 34]. The negative TR value indicates that the response near the rear end of the specimen is less than the response near the loading end of the specimen.

$$TR = 20 \times \log(\frac{\varepsilon_3(f)}{\varepsilon_2(f)}) \tag{3}$$

Where ε_2 and ε_3 are the longitudinal strain at SG2 and SG3 of the tested specimens, respectively; $\varepsilon_1\big|_{peak}$, $\varepsilon_2\big|_{peak}$ and $\varepsilon_3\big|_{peak}$ represent the peak strain value recorded by the attached three gauges, as shown in Fig. 3(b). $\varepsilon_{s1}\big|_{peak}$ is the peak strain recorded in the plain mortar (S-S1) as the reference, and subscript *i* represents the specimen number for each configuration, as shown in Fig. 1; $\varepsilon_2(f)$ is the amplitude of longitudinal strain in the frequency domain recorded by SG2, and $\varepsilon_3(f)$ is the amplitude of longitudinal strain in the frequency domain recorded by SG3.

3.2.1 Response of specimen under non-destructive test (NDT)

The specimens were subsequently investigated under non-destructive tests with the relatively low-amplitude impulses generated by manually striking bar III to bar II (shown in Fig. 3(a)). When the specimen was impacted, the stress waves were generated at the impactor-specimen interface and propagated through the specimen. The primary or longitudinal stress waves then propagated along the loading direction [35]. In order to examine the wave attenuation in the specimens, wave signals near the loading and rear ends were recorded (i.e., $\varepsilon_2(t)$ and $\varepsilon_3(t)$). Fig. 7 shows the strain time histories of $\varepsilon_2(t)$ and $\varepsilon_3(t)$ for seven specimens subjected to non-destructive loading. As shown in Fig. 7(a), there was no apparent wave attenuation in terms of peak strain reduction in S-S1, instead, the strain peak was enlarged. Amplification of the stress was caused by wave interaction (i.e., superposition) between the incident and the reflected wave near the end of the specimen. As shown in Fig. 7(b), the apparent peak stain reduction (i.e., $\varepsilon_3|_{peak} < \varepsilon_2|_{peak}$) was found in S-S2, indicating that the elastic stress waves were attenuated greatly when the waves passed through the RCSBs. Similarly, the value of $\varepsilon_3|_{peak}$ was greatly reduced in S-S3 (Fig. 7(c)) and S-S4 (Fig. 7(d)), demonstrating the metaconcrete specimens consisting of ERCSBs also exhibited favourable wave attenuation properties. Fig. 7(e) shows the strain time histories of plain concrete (i.e., S-S5). It was observed that the value of $\varepsilon_3|_{peak}$ was also higher than $\varepsilon_2|_{peak}$ due to the wave interaction (i.e., superposition). As observed in Fig. 7(f) and (g), the values of $\varepsilon_3|_{peak}$, however, were greatly reduced in S-S6 and S-S7. It can be concluded that all specimens with ERCSBs were capable of mitigating the propagation of elastic stress waves.

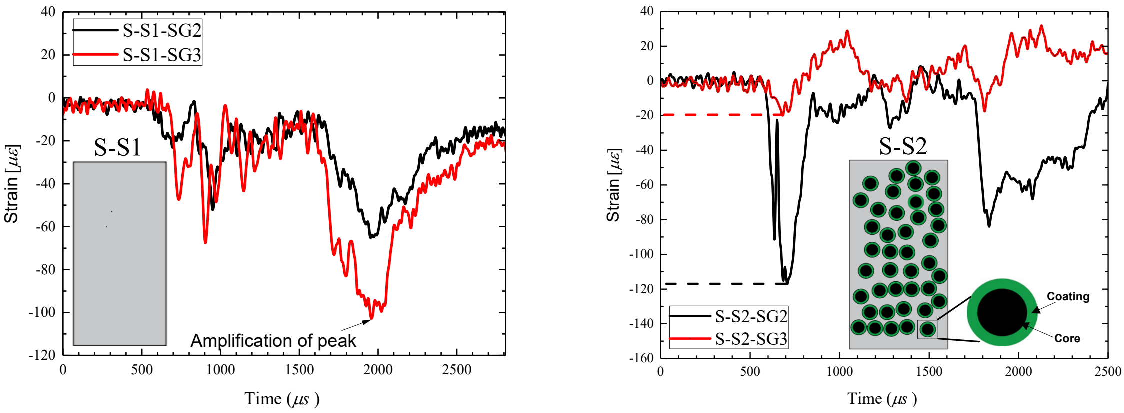

(a) S-S1 (b) S-S2

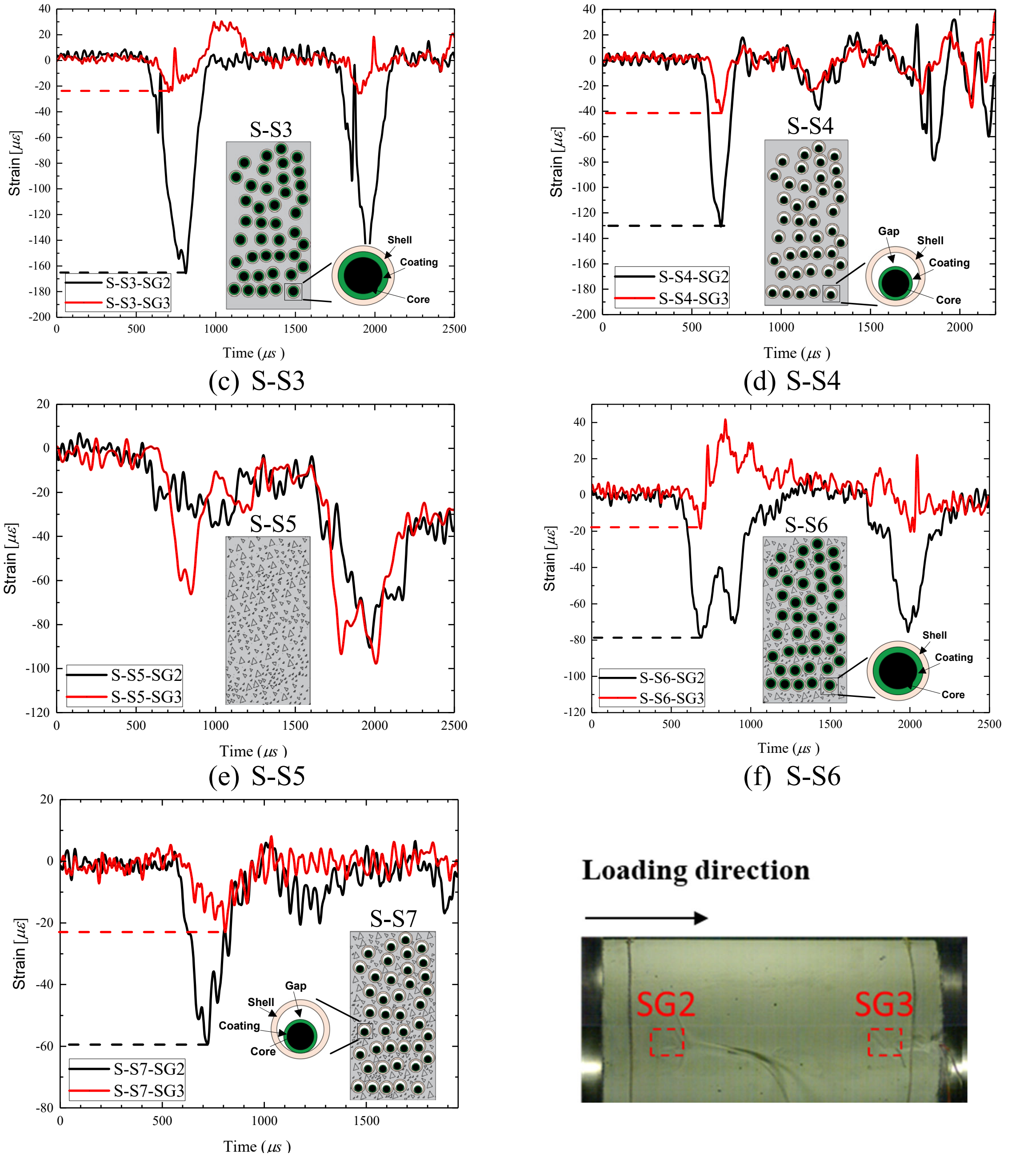

(c) S-S3 (d) S-S4

(e) S-S5 (f) S-S6

(g) S-S7 (h) Strain gauges (SG2/3)

Fig. 7: Strain-time histories of all specimens under non-destructive tests. Note: SG2 and SG3 represent the input and output strain.

Moreover, the performance metric $R_{p\text{-}NDT}$, i.e., peak strain reduction ratio, is summarized in Table 3, where the higher value means superior capacity in attenuating stress wave propagations. By using Eq. (3), the peak strain reduction $R_{p\text{-}NDT}$ of S-S1 was calculated as -27%. The negative value of $R_{p\text{-}NDT}$ signified the magnification of amplitude owing to the superposition of incident and reflected waves. The corresponding one for metaconcrete with RCSBs (S-S2), mortar with ERCSBs/18 (S-S3) and ERCSBs/15 (S-S4) was 79%, 86% and

62%, respectively, as listed in Table 3. S-S3 showed a higher $R_{p\text{-}NDT}$ than S-S2 owing to the more pronounced difference of wave impedances between steel shell and mortar matrix as compared to that between rubber coating and mortar matrix. When elastic wave approaches the interface between steel shell and cementitious matrix with different impedances, the incident stress wave partially reflects and the rest refracts into other material [36]. As a result, more stress wave attenuation can be achieved. S-S3 also presented a higher value of $R_{p\text{-}NDT}$ than S-S4 because the steel core inside ERCSBs/18 was larger than that inside ERCSBs/15. S-S3 also displayed a higher $R_{s\text{-}NDT}$ (i.e., the specific reduction ratio of strain with respect to plain mortar) of 422% than 396% of S-S2 and 332% of S-S4, as calculated by Eq. (4). Table 3 tabulates the values of $R_{p\text{-}NDT}$ and $R_{s\text{-}NDT}$ for S-S5, S-S6 and S-S7. Among concrete-based specimens, S-S6 had the highest reduction values of 71% ($R_{p\text{-}NDT}$) and 365% ($R_{s\text{-}NDT}$), which were greater than S-S5 of -0.4% and 98% as well as S-S7 of 68% and 354%, respectively. Based on the above results, it can be concluded that using the enhanced EAs proposed in this study can achieve comparable or even slightly better wave propagation attenuation than the conventional EAs, and the design of ERCSB/18 performed better than ERCSB/15, indicating the idea of allowing RCSB sliding inside the steel shell did not lead to better energy absorption probably because the steel core vibration in RCSB was less excited.

Furthermore, the wave attenuation mechanism associated with the above observation could be inferred from the frequency domain analysis, which has been widely used in previous studies [16-18]. The transmission ratio (TR) with respect to the longitudinal strain was calculated by Eq. (5). The curves of TR versus frequencies ranged from 0 kHz to 15 kHz for S-S1 to S-S4 are presented in Fig. 8. As shown in Fig. 8(a), there was no significant drop in spectral amplitudes in the TR curve of the plain mortar (S-S1), implying that no noticeable wave filtering effect was found. S-S2 with randomly dispersed RCSBs displayed a frequency-dependent attenuation, in which a minimum TR value of -32.8 dB at 3.6 kHz (i.e., frequency dip) was observed. Therefore, the local resonance effect played an important role in mitigating stress wave propagation. As the loading frequency approached the resonant frequency of RCSBs, a large proportion of wave energy was transferred to the local vibration of the cores, which reduced the wave energy transmitting across the mortar matrix. This attenuation phenomenon was consistent with the experimental results reported in the previous studies [14-17]. As compared to S-S2, both S-S3 and S-S4 exhibited analogous frequency-depended attenuation effects. For S-S3 with ERCSBs/18, an apparent frequency dip occurred at 5.6 kHz as shown in Fig. 8(a), in which the minimum TR was around -41.0 dB. Similar to S-S2, the local resonance of the core inside ERCSBs could dissipate wave energy, resulting in favourable wave attenuation performance. In addition, S-S4 displayed a less significant attenuation effect in which the minimum TR was around -39.9 dB at 8.8 kHz. The frequency-dependent wave-filtering capacity and attenuation behaviours found in S-S3 and S-S4 with ERCSBs, as well as in S-S2, can be attributed to the local resonance effect. Likewise, the frequency spectra for concrete-based specimens are shown in Fig. 8(b). There was no substantial reduction regarding spectral amplitude of plain concrete (S-S5) owing to the nonexistence of local resonant aggregates. In contrast, apparent frequency dips were observed in S-S6 and S-S7, in which the minimum TR was around -36.5 dB at 5.8 kHz and -33.6 dB at 8.9 kHz, respectively. Again, metaconcrete consisting of both conventional (i.e., RCSBs) and enhanced EAs (i.e., ERCSBs) showed the frequency-dependent wave-filtering effect within the prescribed frequency range or bandgap. Specifically, the EAs tuned within the prescribed bandgap led to an out-of-phase vibration of the inner metal core. This local vibration of the core could interact with stress waves induced by impulsive loading, hence mitigating the stress wave propagation through the matrix. The details of deriving the prescribed frequency range were not presented herein but can refer to the previous studies [9, 20, 21]. In conclusion, adding ERCSBs was effective for elastic wave propagation attenuation under the non-destructive impulsive load.

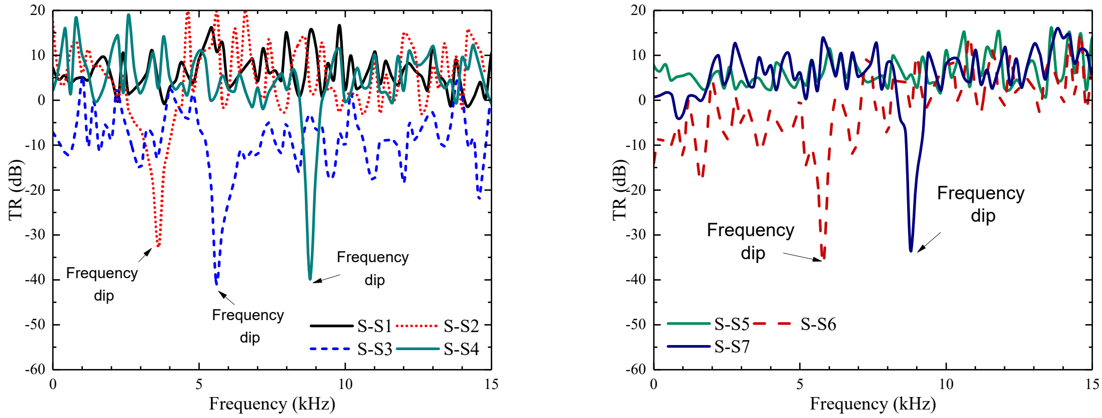

(a) Mortar-based specimen (b) Concrete-based specimen

Fig. 8: Comparisons of transmission ratio (TR) of different specimens.

3.2.2 Response of specimens under destructive test (DT)

Fig. 3(b) shows the setup of the destructive test. It is worth mentioning that this experiment focused on the effectiveness in mitigating stress wave propagation of each specimen rather than its dynamic material properties. Stress equilibrium condition [37] was thus not required for this test. Besides, three loading cases with different peak incident stress (i.e., impulses I, II and III as shown in Fig. 9 by varying striker velocities through changing air pressure in the pressure vessel) were utilized to examine the dynamic responses of each specimen.

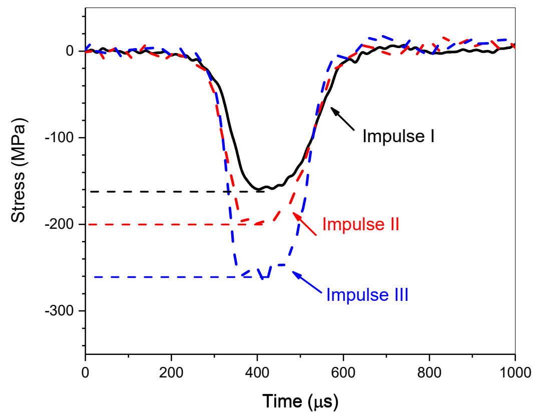

Fig. 8: Typical input impulses I, II and III.

3.2.2.1 Failure process and failure modes

The typical failure process of all the specimens under intermediate impulsive loads (impulse II) is shown in Fig. 10(a) and (b) captured by using a high-speed camera. For impulse I, specimens experienced less severe damage while specimens were rapidly pulverized into fragments under impulsive III. To better demonstrate the damage initiation and development before the specimens completely failed, the failure processes subjected to impulse II were demonstrated herein. 0 μs represented the moment when the specimen was initially stressed. For plain mortar (S-S1), cracks initiated from the loading side of the specimens and developed into the mid-region. Afterwards, more cracks initiated within the mid-region and developed further. As shown in Fig. 10(a), S-S1 experienced spall damage, i.e., clear tensile damage, owing to the reflected stress wave. This damage mode of plain mortar was consistent with the experimental results reported in the previous study [37, 38]. Metaconcrete with RCSBs developed cracks earlier than the plain mortar due to its lower compressive strength, i.e., S-S2 showed severe cracks in the middle region at 320 μs, while only minor crack was found on the S-S1 at 320 μs. In addition, metaconcrete with RCSBs suffered severe failure as shown in Fig. 10(a), the cracks were parallel to the loading direction concentrated in the middle region, showing a splitting failure mode. S-S2 at 640 μs showed more cracks than S-S1 at the same time instant. At 640 μs, two major cracks were nearly parallel to the loading direction together with numerous minor cracks extended from arbitrary directions as observed in Fig. 10(a). Severe diagonal fractures were observed in S-S2 at 960 μs owing to its low compressive strength.

For the metaconcrete specimen with ERCSBs/18 (S-S3), the cracks initiated at the loading surface of the specimen and propagated to the middle region at 320 μs. Besides, the number of cracks at all-time instants for S-S3 was less than that of the metaconcrete with RCSBs (S-S2) owing to the higher compressive strength of S-S3. S-S4 also experienced fewer cracks than S-S2 at all-time instants due to the existence of hard steel shells. The previous study [12, 18] reported that the effect of local oscillation of heavy cores may lead to a reduction in the crack development as the local vibration of EAs could dissipate a certain amount of wave energy. However, S-S2 displayed lower resistance and less mitigation capacity due to early damage to the matrix. By adding steel shells, the mitigation capacity and damage resistance were improved as compared to metaconcrete with RCSBs (S-S2). Eventually, both S-S1 and S-S2 were shattered into small pieces because of the brittle nature of the mortar matrix as shown in Fig. 11(a). In contrast, the majority part of metaconcrete specimens with ERCSBs (i.e., S-S3 and S-S4) remained intact. It is also noted that no tensile crack was observed in S-S3 and S-S4, implying the ERCSBs reduced the stress wave amplitude such that the reflected tensile stress wave was small to cause tensile failure in S-S3 and S-S4.

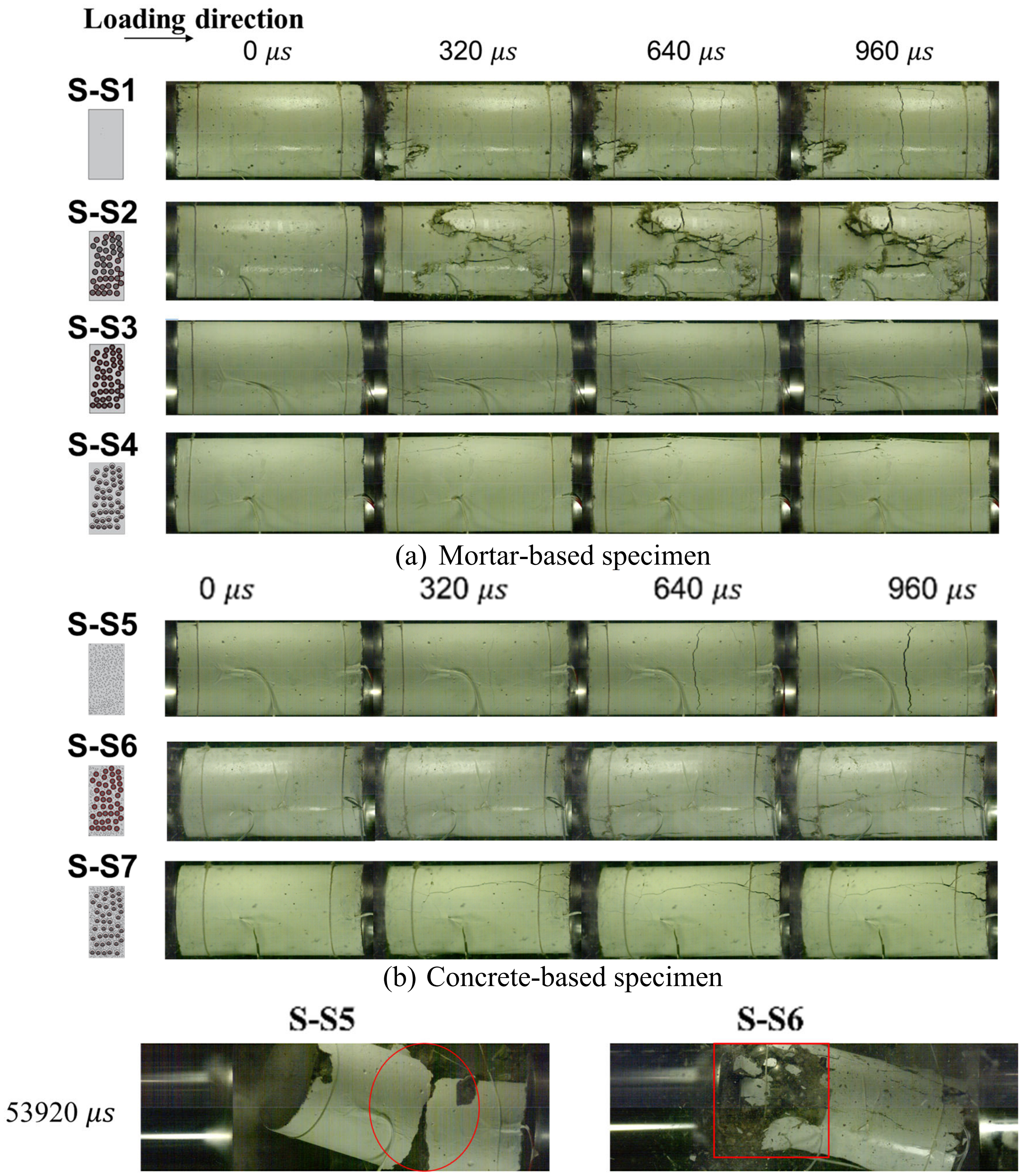

(a) Mortar-based specimen

(b) Concrete-based specimen

(c) Failure process comparison of S-S5 and S-S6 under impulse II

Fig. 9: Failure process of specimens subjected to impulse II.

The fracture pattern observed in the plain concrete (i.e., S-S5) was similar to S-S1 under impulse II. As shown in Fig. 10(b) and (c), the plain concrete specimen was broken into two parts owing to tensile failure. This damage mode of plain concrete was consistent with the experimental results reported in the previous study [37, 39, 40]. For metaconcrete (i.e., S-S6 and S-S7), however, it experienced brittle crushing damage on the loading end as shown in Fig. 10(c). It is noteworthy that cracks in specimens usually initiated at weak sections (i.e., ITZ or air voids) and then extended. For metaconcrete with ERCSBs, the induced cracks in the specimens associated with impulsive loads were originated from the interface between ERCSBs and the surrounding matrix and then propagated either parallel (i.e., longitudinal cack) or perpendicular (i.e., transverse crack) to the loading direction. As shown in Fig. 10(c), SS-S5 experienced dynamic fracture (i.e., spalling) in the middle at the time instant of 53920 μs and S-S6 experienced severe crushing at the loading end at the same instant, which could absorb a significant amount of energy and result in less amount of wave energy transmitting to the remaining part of the specimen. Based on the above observations, it can be concluded that mixing EAs with a stiff shell in metaconcrete greatly enhanced the structural capacity to resist impulsive loads.

Fig. 11 shows the final failure modes of the specimens with various configurations under different input loads (impulses I, II and III). As observed, plain mortar (S-S1) and plain concrete (S-S5) experienced significant dynamic fracture (i.e., spalling) and they were disintegrated into two parts under impulse I owing to insufficient tensile strength. These failure modes of plain mortar and concrete were consistent with the experimental results reported in the previous studies [37, 38, 40], and the fracture profile agreed with the results reported by Klepaczko and Brara [39]. Metaconcrete with RCSBs (S-S2) experienced columnar cracking through both ends, and severe localized damage was found in the middle region due to stress concentration at the interfacial area around RCSBs. This damage mode was also consistent with the results reported in the previous studies [6, 7, 18]. Besides, metaconcrete with both types of ERCSBs (i.e., S-S3, S-S4, S-S6 and S-S7) experienced localized damage and only several cracks appeared near the loading end under impulse I, as illustrated in Fig. 11(a) and (b). Based on the above results, metaconcrete with ERCSBs demonstrated better impulsive loading resistance as compared to metaconcrete with RCSBs (S-S2) as well as plain specimens (S1-S1 and S-S5) under impulse I.

With the applied load increased to impulse II, plain mortar (S-S1) was shattered into several fragments as shown in Fig. 11(a). Metaconcrete with RCSBs (S-S2) exhibited unsatisfactory loading resistance, in which the diagonal fracture with several cracks through the rear ends was observed and the front part was crushed into numerous pieces owing to its lower compressive strength. For S-S3 under impulse II, it experienced damage in the middle region and an obvious crack was observed perpendicular to the loading direction but the overall specimen was still intact. For S-S4, a relatively large piece at the mid-section of the specimen fell off while the rest of the part was intact. Thus, metaconcrete specimens with ERCSBs/18 and ERCSBs/15 had higher loading resistance as compared to other specimens (S-S1 and S-S2) under impulse II as these specimens were shattered into small pieces. Plain concrete (S-S5) was broken into two disconnected parts under impulse II owing to the reflected tensile stress wave. As shown in Fig. 11(b), approximately 1/3 of S-S6 on the loading side was crushed but the remaining part of the specimen kept its integrity with some peel-off damage on the specimen surface. S-S7 also experienced local damage near the loading end. Peel-off damage to the specimen appeared more severe in S-S3, S-S4, S-S6 and S-S7. This could be attributed to poor bonding between steel shell and mortar matrix. Under axial impact loading, the specimens expanded laterally owing to Poisson’s ratio effect, poor bonding between mortar and EAs caused the specimen more vulnerable to the peel-off damage. Therefore, improving the bonding strength between EA and mortar matrix is important. Moreover, peel-off damage may be caused by the wave impedance mismatch between steel shell and cementitious matrix, so that significant wave reflection was induced leading to serious interfacial failure. Hence, the enhanced coating material with wave impedance closed to the matrix material is suggested to ensure smooth transmission of stress waves inside the engineered aggregate, which could potentially reduce the interfacial failure.

Higher loading intensity greatly affected the failure mode of metaconcrete. Under impulse I and II, a certain level of specimen integrity was maintained. When a more intensive load (i.e., impulse III) was applied, all the specimens were shattered into smaller pieces. For instance, S-S1 was crushed into chunks, while metaconcrete with RCSBs, ERCSBs/18 and ERCSBs/15 broke into various pieces, as shown in Fig. 11(a) and (b). Smaller fragments (broken pieces) were generated in metaconcrete than plain specimens owing to its insufficient interfacial strength between EAs and cementitious matrix. Based on the above results, metaconcrete consisting of EAs with the enhanced coating (i.e., ERCSBs) showed a higher loading resistance capacity than metaconcrete with RCSBs in all loading cases.

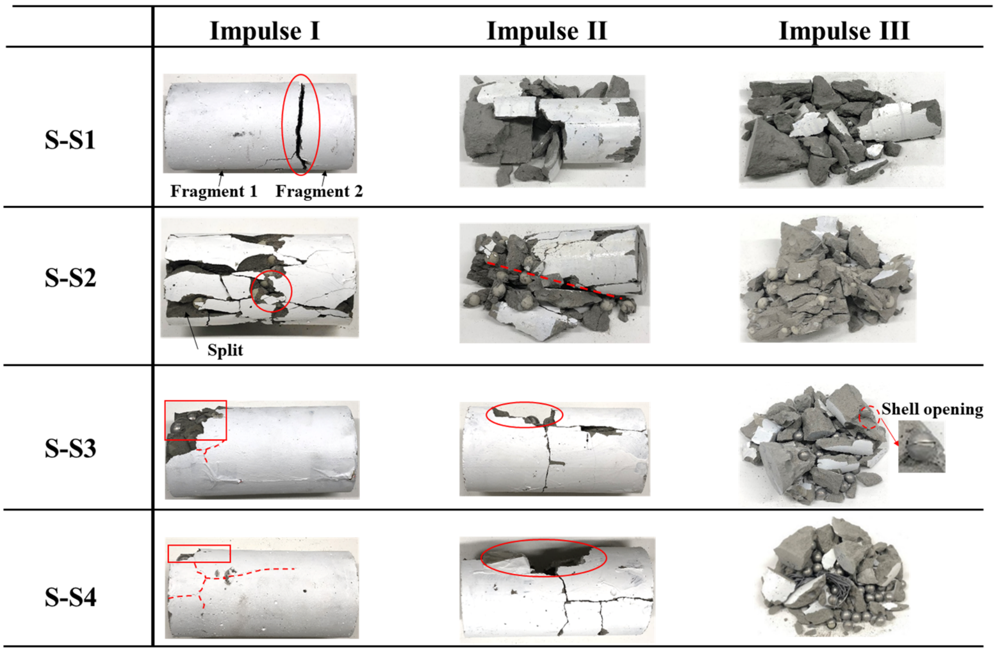

(a) Mortar-based specimen

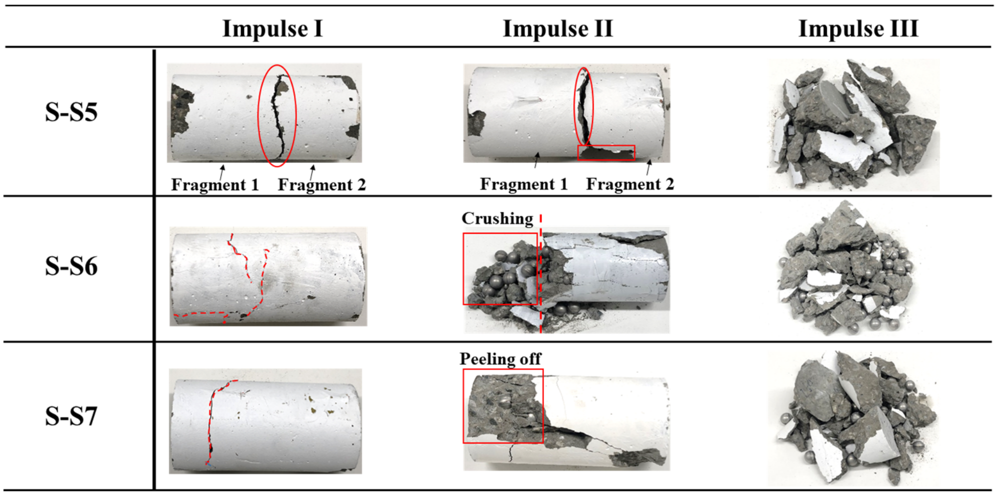

(b) Concrete-based specimen

Fig. 10: Failure modes of specimens subjected to impulses I, II and III.

3.2.2.2 Comparison of stress wave attenuation performance

To further examine the effectiveness of wave attenuation in metaconcrete and plain specimens, strain-time histories for all the specimens subjected to impulses I, II and III are compared in Fig. 12. S-S2 had the highest value of $\varepsilon_2|_{peak}$ owing to its lowest modulus of elasticity or stiffness of the material, as shown in Fig. 12(b). Meanwhile, the strain gauge near the loading end (i.e., SG2) was broken at an early stage because of the specimen damage (see Fig. 10(a)), which was due to its lower compressive strength when subjected to impulses I, II and III. As shown in Fig. 12(c) and (d), S-S3 and S-S4 had smaller values of $\varepsilon_2|_{peak}$ as compared to S-S1 owing to their higher modulus of elasticity. It is worth noting that the stress wave propagating along the specimen was inhibited if a substantial reduction in the transmitted peak strain (i.e., SG3) was obtained. No significant peak strain reduction indicated that there was no noticeable stress wave attenuation effect, whereas a noticeable reduction of peak transmitted strain ($\varepsilon_3|_{peak}$) indicated the wave propagation mitigation. As shown in Fig. 12(a), S-S1 exhibited no significant wave attenuation effect as the reduction of transmitted peak strain was not obvious for each loading scenario. In contrast, noticeable peak strain reduction was found in S-S2 (see Fig. 12(b)), implying that the stress wave was attenuated after passing through the conventional RCSBs owing to the local resonance effect, in which this attenuation phenomenon was consistent with the experimental observation reported in the previous study [18]. Besides, considerable peak strain reduction was also observed in S-S3 and S-S4 (see Fig. 12(c) and (d)), demonstrating the addition of a hard shell did not significantly affect the wave mitigation performance of the engineered aggregates. In fact, ERCSB could provide a comparable or even better wave mitigation effect than conventional RCSB. For plain concrete (S-S5), the value of peak transmitted strain ($\varepsilon_3\big|_{peak}$) was close to the peak incident value ($\varepsilon_2\big|_{peak}$), namely, there was no noticeable wave propagating attenuation, as observed in Fig. 12(e). In contrast, the values of $\varepsilon_3\big|_{peak}$ for S-S6 and S-S7, as displayed in Fig. 12(f) and (g), were considerably reduced, indicating the specimens with ERCSBs achieved stress wave attenuation performance than plain concrete due to the local resonance of engineered aggregates. To conclude, metaconcrete consisting of enhanced EAs proposed in this study can improve the strength of metaconcrete and also maintain its stress wave attenuation capacity.

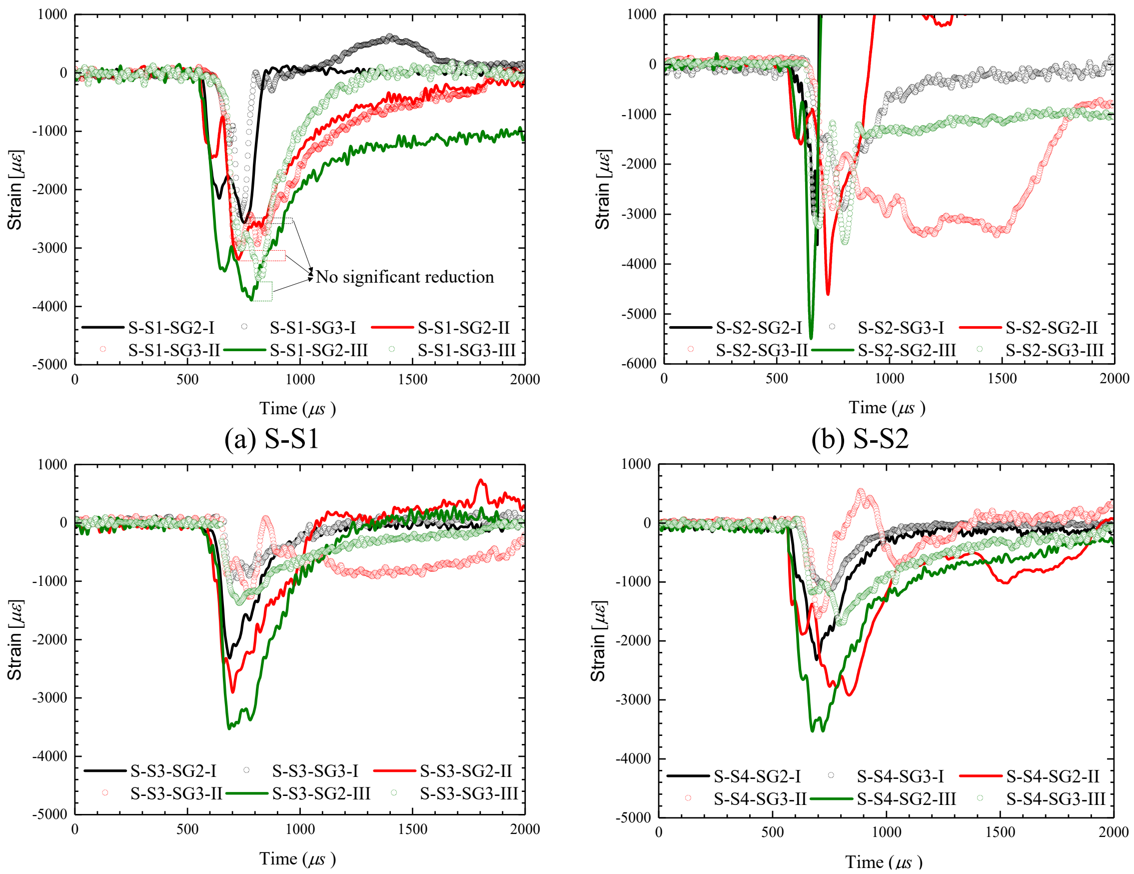

(a) S-S1 (b) S-S2

(c) S-S3 (d) S-S4

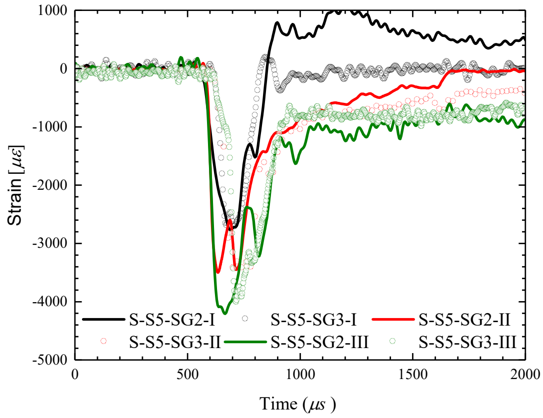

(e) S-S5

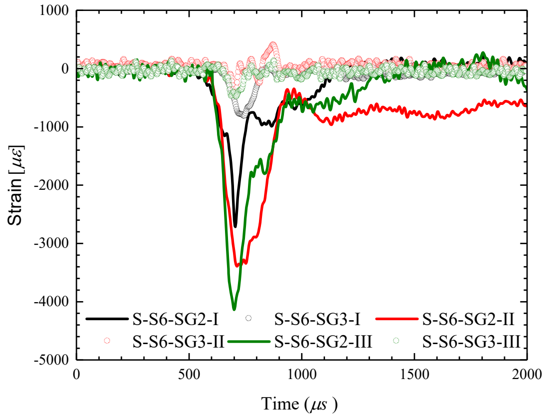

(f) S-S6

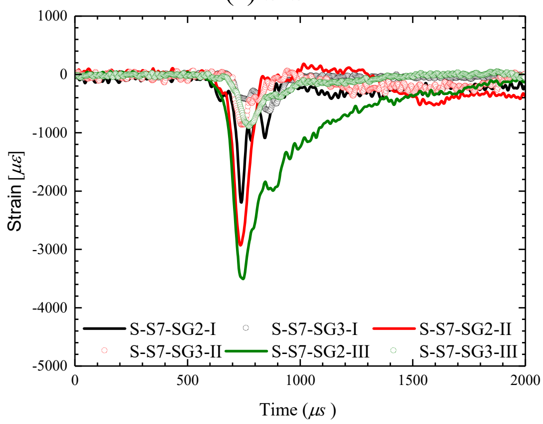

(g) S-S7

Fig. 11: Comparison of strain-time histories of specimens subjected to impulses I, II and III.

Moreover, the peak reduction ratios of the maximum longitudinal strain ($R_{p\text{-}DT}$) derived by using Eq. (3) are summarized in Table 5 to qualitatively compare the performance of wave propagation mitigation. A higher value of $R_{p\text{-}DT}$ indicated a greater reduction in the maximum longitudinal strain within the specimen, namely better wave propagation mitigation performance. As shown in Table 5, the specimen with RCSBs generally had a greater value of $R_{p\text{-}DT}$ than the plain specimens (e.g., S-S1) in all loading cases. For instance, $R_{p\text{-}DT}$ under impulses I, II and III in S-S2 was 20%, 26% and 35%, which were greater than S-S1 of 5%, 6% and 8%, respectively. This was because the local resonance of the core attenuated the stress waves propagating through the specimen. However, owing to the lower strength of metaconcrete with RCSBs, S-S2 experienced severe damage to the surrounding matrix at an early stage, which limited the activation of local resonance. This observation was consistent with those reported in the previous numerical studies [6, 9]. Thus, its wave propagation attenuation effect was not significant as compared to metaconcrete with ERCSBs. By adding a steel shell, metaconcrete with ERCSBs showed a higher reduction value. For instance, $R_{p\text{-}DT}$ of S-S3 under impulses I, II and III were 52%, 57% and 61%, which were greater than S-S2 of 20%, 26% and 35%, respectively, as given in Table 5. This was because metaconcrete with ERCSBs had higher strength, which prolonged the local resonance effect and led to a better mitigation performance. Besides, S-S3 generally had a higher $R_{p\text{-}DT}$ value than S-S4. This was because ERCSBs/18 with a larger steel core than ERCSBs/15 resulted in a more prominent local resonance effect, and the gap between RCSB and steel shell in ERCSB/15 might also lead to the less activated steel core vibration as discussed above. In addition, as shown in Fig. 10, localized matrix material damage could also dissipate energy and a lower proportion of input energy were transmitted to the rest part of the specimen. For instance, the front parts of S-S6 and S-S7 were significantly crushed and the rest parts experienced less damage. The failure of the front part dissipated a large amount of energy, which resulted in a lower proportion of energy being transmitted to the rest part. Therefore, the energy dissipation was contributed by the matrix fracture damage and the local resonance effect. As given in Table 5, $R_{p\text{-}DT}$ was 70%, 89% and 90% for S-S6, and 60%, 70% and 75% for S-S7, which were substantially greater than 1.7%, 2% and 5% of S-S5 (i.e., plain concrete). Furthermore, with the increased loading intensity (i.e., from impulse I to III), $R_{p\text{-}DT}$ gradually increased for metaconcrete with ERCSBs. It can be explained as follows: a) higher loading amplitude induced larger local vibrations of hard core inside engineered aggregate so that more wave energy was absorbed by the engineered aggregates [9, 20]; b) more severe matrix material damage with the rising loading intensity could dissipate substantial amounts of energy; c) damage of steel shell (e.g., shell opening) outside the ERCSBs (see Fig. 11) could also absorb considerable amounts of wave energy leading to more effective mitigation effect.

As given in Table 5, $R_{s\text{-}DT}$ (i.e., the specific reduction ratio of strain with respect to plain mortar) slightly varied for metaconcrete with ERCSBs under different loading scenarios. Metaconcrete with ERCSBs had a higher value of $R_{s\text{-}DT}$ than metaconcrete with RCSBs and followed by plain mortar and plain concrete. For instance, by using Eq. (4), a similar trend for the value of $R_{s\text{-}DT}$ was observed in all specimens. Especially, when subjected to impulse II, S-S6 had the highest $R_{s\text{-}DT}$ of 93%, followed by S-S7 of 91%, S-S3 of 89% and S-S4 of 87%. $R_{s\text{-}DT}$ of S-S5 was calculated as -200%, indicating S-S5 ($R_{p\text{-}DT}$ = 2%) had a lower mitigation capacity of stress wave propagation than S-S1 ($R_{p\text{-}DT}$ = 6%) as given in Table 5. It should be noted that the negative value of $R_{s\text{-}DT}$ indicates the level of stress wave propagation mitigation in the specific specimen was less than that in the reference specimen (S-S1).

Table 5: Summary of destructive testing (DT) results under impulses I, II and III.

No.	**Specimen**	$R_{p\text{-}DT}$			$R_{s\text{-}DT}$		
		I	**II**	**III**	**I**	**II**	**III**
S-S1	Plain mortar	5%	6%	8%	-	-	-
S-S2	Mortar with RCSBs	20%	26%	35%	73%	77%	75%
S-S3	Mortar with ERCSBs/18	52%	57%	61%	90%	89%	86%
S-S4	Mortar with ERCSBs/15	40%	47%	52%	87%	87%	84%
S-S5	Plain concrete	1.7%	2%	5%	-174%	-200%	-73%
S-S6	Concrete with ERCSBs/18	70%	89%	90%	92%	93%	91%
S-S7	Concrete with ERCSBs/15	60%	70%	75%	91%	91%	89%

Note: "-" means reference specimen (S-S1).

4 Conclusion

In this study, a new kind of engineered aggregate (ERCSB) was proposed to enhance the mechanical properties of conventional metaconcrete. Quasi-static mechanical properties and dynamic responses of plain mortar, normal concrete and metaconcrete with RCSBs or ERCSBs under destructive and non-destructive dynamic loads were experimentally investigated. The experimental results confirmed the effectiveness of using ERCSBs in metaconcrete in enhancing the compressive strength while preserving the wave attenuation ability in comparison with metaconcrete with conventional RCSBs. The main findings from this study are summarised as follows.

1. Metaconcrete with randomly dispersed RCSBs could exhibit frequency-dependent attenuation properties, which can mitigate elastic and inelastic stress wave propagation owing to the local resonance effect.
2. The quasi-static compressive property of metaconcrete with RCSBs was reduced due to the soft coating of conventional EAs (RCSBs). It can be addressed by adding a hard shell outside RCSBs to form ERCSBs, which can increase metaconcrete's compressive strength by 80.3 % and modulus of elasticity by 72.3% as compared to the metaconcrete with RCSBs.
3. Metaconcrete with ERCSBs also exhibited frequency-dependent wave filtering capacity, resulting in favourable wave attenuation performance. The specimens with both types of ERCSBs (without/with a gap between the external shell and RCSB) were effective in mitigating stress wave propagation induced by non-destructive and destructive dynamic loads.
4. Insufficient bonding between the matrix and EAs negatively impacted on both the static mechanical properties and dynamic responses of metaconcrete. To improve the performance of metaconcrete, mechanical or chemical treatment on ERCSBs' outer layer is recommended to improve its bonding strength.

Declaration of Competing Interest

The author(s) declared no potential conflicts of interest with respect to the research, authorship and/or publication of this article.

Acknowledgement

The authors acknowledge the support from the Australian Research Council to conduct this research work. The first author also acknowledges support through the Australian Government Research Training Program Scholarship.

References

[1] Cheng Z, Shi Z. Novel composite periodic structures with attenuation zones. Engineering Structures. 2013;56:1271-82.

[2] Muhammad, Lim CW, Reddy JN. Built-up structural steel sections as seismic metamaterials for surface wave attenuation with low frequency wide bandgap in layered soil medium. Engineering Structures. 2019;188:440-51.

[3] Cheng Z, Shi Z, Palermo A, Xiang H, Guo W, Marzani A. Seismic vibrations attenuation via damped layered periodic foundations. Engineering Structures. 2020;211:110427.

[4] Zhang K, Luo J, Hong F, Deng Z. Seismic metamaterials with cross-like and square steel sections for low-frequency wide band gaps. Engineering Structures. 2021;232:111870.

[5] Muhammad, Lim CW, Kamil Żur K. Wide Rayleigh waves bandgap engineered metabarriers for ground born vibration attenuation. Engineering Structures. 2021;246:113019.

[6] Jin H, Hao H, Hao Y, Chen W. Predicting the response of locally resonant concrete structure under blast load. Construction and Building Materials. 2020;252:118920.

[7] Jin H, Hao H, Chen W, Xu C. Spall Behaviors of Metaconcrete: 3D Meso-Scale Modelling. International Journal of Structural Stability and Dynamics. 2021:2150121.

[8] Xu C, Chen W, Hao H. The influence of design parameters of engineered aggregate in metaconcrete on bandgap region. Journal of the Mechanics and Physics of Solids. 2020:103929.

[9] Xu C, Chen W, Hao H, Jin H. Effect of engineered aggregate configuration and design on stress wave attenuation of metaconcrete rod structure. International Journal of Solids and Structures. 2021;232:111182.

[10] Mitchell SJ, Pandolfi A, Ortiz M. Metaconcrete: designed aggregates to enhance dynamic performance. Journal of the Mechanics and Physics of Solids. 2014;65:69-81.

[11] Mitchell SJ, Pandolfi A, Ortiz M. Investigation of elastic wave transmission in a metaconcrete slab. Mechanics of Materials. 2015;91:295-303.

[12] Mitchell SJ, Pandolfi A, Ortiz M. Effect of Brittle Fracture in a Metaconcrete Slab under Shock Loading. Journal of Engineering Mechanics. 2016;142:04016010.

[13] Tan SH, Poh LH, Tkalich D. Homogenized enriched model for blast wave propagation in metaconcrete with viscoelastic compliant layer. International Journal for Numerical Methods in Engineering. 2019;119:1395-418.

[14] Briccola D, Ortiz M, Pandolfi A. Experimental Validation of Metaconcrete Blast Mitigation Properties. Journal of Applied Mechanics. 2016;84:031001--6.

[15] Briccola D, Tomasin M, Netti T, Pandolfi A. The Influence of a Lattice-Like Pattern of Inclusions on the Attenuation Properties of Metaconcrete. Frontiers in Materials. 2019;6.

[16] Briccola D, Cuni M, De Juli A, Ortiz M, Pandolfi A. Experimental Validation of the Attenuation Properties in the Sonic Range of Metaconcrete Containing Two Types of Resonant Inclusions. Experimental Mechanics. 2020.

[17] Briccola D, Pandolfi A. Analysis on the Dynamic Wave Attenuation Properties of Metaconcrete Considering a Quasi-Random Arrangement of Inclusions. Frontiers in Materials. 2021;7.

[18] Kettenbeil C, Ravichandran G. Experimental investigation of the dynamic behavior of metaconcrete. International Journal of Impact Engineering. 2018;111:199-207.

[19] Liu Y, An X, Chen H, Fan H. Vibration attenuation of finite-size metaconcrete: Mechanism, prediction and verification. Composites Part A: Applied Science and Manufacturing. 2021;143:106294.

[20] Xu C, Chen W, Hao H, Bi K, Pham TM. Experimental and numerical assessment of stress wave attenuation of metaconcrete rods subjected to impulsive loads. International Journal of Impact Engineering. 2022;159:104052.

[21] Xu C, Chen W, Hao H, Pham TM, Bi K. Damping properties and dynamic responses of metaconcrete beam structures subjected to transverse loading. Construction and Building Materials. 2021;311:125273.

[22] Davco Australia. Davco lanko 701 duragrout data sheet. 2020.

[23] ASTM C29 / C29M-07. Standard Test Method for Bulk Density (Unit Weight) and Voids in Aggregate. West Conshohocken, PA: ASTM International; 2007.

[24] Kim KM, Lee S, Cho JY. Effect of maximum coarse aggregate size on dynamic compressive strength of high-strength concrete. International Journal of Impact Engineering. 2019;125:107-16.

[25] Gagnon L, Morandini M, Ghiringhelli GL. A review of particle damping modeling and testing. Journal of Sound and Vibration. 2019;459:114865.

[26] Masri SF, Ibrahim AM. Response of the impact damper to stationary random excitation. The Journal of the Acoustical Society of America. 1973;53:200-11.

[27] Salueña C, Pöschel T, Esipov SE. Dissipative properties of vibrated granular materials. Physical Review E. 1999;59:4422-5.

[28] Lu Z-Q, Zhao L, Ding H, Chen L-Q. A dual-functional metamaterial for integrated vibration isolation and energy harvesting. Journal of Sound and Vibration. 2021;509:116251.

[29] ASTM C192/C192M-19. Standard Practice for Making and Curing Concrete Test Specimens in the Laboratory. West Conshohocken, PA: ASTM International; 2019.

[30] ASTM C39/C39M-21. Standard Test Method for Compressive Strength of Cylindrical Concrete Specimens. West Conshohocken, PA: ASTM International; 2021.

[31] ASTM C469/C469M-14e1. Standard Test Method for Static Modulus of Elasticity and Poisson's Ratio of Concrete in Compression. West Conshohocken, PA: ASTM International; 2014.

[32] Pham TM, Chen W, Khan AM, Hao H, Elchalakani M, Tran TM. Dynamic compressive properties of lightweight rubberized concrete. Construction and Building Materials. 2020;238:117705.

[33] Chen X, Wu S, Zhou J. Experimental and modeling study of dynamic mechanical properties of cement paste, mortar and concrete. Construction and Building Materials. 2013;47:419-30.

[34] Matlack KH, Bauhofer A, Krödel S, Palermo A, Daraio C. Composite 3D-printed metastructures for low-frequency and broadband vibration absorption. Proceedings of the National Academy of Sciences. 2016;113:8386-90.

[35] McVay MK. Spall damage of concrete structures. Waterways Experiment Station, Vicksburg, Miss: Army Corps of Engineers; 1988.

[36] Wang L. Foundations of stress waves. Amsterdam: Elsevier Science Ltd; 2007.

[37] Brara A, Camborde F, Klepaczko JR, Mariotti C. Experimental and numerical study of concrete at high strain rates in tension. Mechanics of Materials. 2001;33:33-45.

[38] Khosravani MR, Wagner P, Fröhlich D, Weinberg K. Dynamic fracture investigations of ultra-high performance concrete by spalling tests. Engineering Structures. 2019;201:109844.

[39] Klepaczko JR, Brara A. An experimental method for dynamic tensile testing of concrete by spalling. International Journal of Impact Engineering. 2001;25:387-409.

[40] Wu H, Zhang Q, Huang F, Jin Q. Experimental and numerical investigation on the dynamic tensile strength of concrete. International Journal of Impact Engineering. 2005;32:605-17.